

Title: T₁, diffusion tensor, and quantitative magnetization transfer imaging of the hippocampus in an Alzheimer's disease mouse model

Article Type: Original Contribution

Authors: Heather T. Whittaker*,^{a,b} Shenghua Zhu,^c Domenico L. Di Curzio,^d Richard Buist,^e Xin-Min Li,^f Suzanna Noy,^b Frances K. Wiseman,^b Jonathan D. Thiessen,^{g,h} and Melanie Martin^{c,e,i}

Author Affiliations:

^aBiopsychology, University of Winnipeg, Winnipeg, MB, R3B 2N2, Canada

^bNeurodegenerative Disease, University College London Institute of Neurology, London, WC1N 3BG, United Kingdom

^cPharmacology and Therapeutics, University of Manitoba, Winnipeg, MB, R3E 0T6, Canada

^dPathology, University of Manitoba, Winnipeg, MB, R3E 3P5, Canada

^eRadiology, University of Manitoba, Winnipeg, MB, R3E 0T6, Canada

^fPsychiatry, University of Alberta, Alberta, T6G 2R3, Canada

^gImaging Program, Lawson Health Research Institute, London, ON, N6A 4V2, Canada

^hMedical Biophysics, Western University, London, Ontario, Canada,

ⁱPhysics, University of Winnipeg, R3B 2N2, Canada

*Corresponding Author:

Heather T. Whittaker

Email: whittaker-h@webmail.uwinnipeg.ca

Phone: 1-204-786-9442

Fax: 1-204-774-4134

Present Address: Faculty of Medicine, McGill University, Montreal, QC, H3A 2R7 Canada

Word count of abstract: 163

Word count of text: 5,562

Number of text pages: 16

Number of figures: 5

Number of tables: 3

Number of references: 68

Abstract

Alzheimer's disease (AD) pathology causes microstructural changes in the brain. These changes, if quantified with magnetic resonance imaging (MRI), could be studied for use as an early biomarker for AD. The aim of our study was to determine if T₁ relaxation, diffusion tensor imaging (DTI), and quantitative magnetization transfer imaging (qMTI) metrics could reveal changes within the hippocampus and surrounding white matter structures in *ex vivo* transgenic mouse brains overexpressing human amyloid precursor protein with the Swedish mutation. Delineation of hippocampal cell layers using DTI color maps allows more detailed analysis of T₁-weighted imaging, DTI, and qMTI metrics, compared with segmentation of gross anatomy based on relaxation images, and with analysis of DTI or qMTI metrics alone. These alterations are observed in the absence of robust intracellular A β accumulation or plaque deposition as revealed by histology. This work demonstrates that multiparametric quantitative MRI methods are useful for characterizing changes within the hippocampal substructures and surrounding white matter tracts of mouse models of AD.

Highlights

- *ex vivo* transgenic mouse brains contained regional differences in multiple quantitative MRI metrics
- DTI color maps are useful for manual segmentation of hippocampal substructures
- more significant differences in quantitative MRI metrics were found in hippocampal cell layers than in the whole hippocampus

Keywords: dementia; quantitative magnetic resonance imaging; multiparametric; diffusion; animal model; *ex vivo*

1. Introduction

As the global population ages and faces an increasing prevalence of Alzheimer's disease (AD), the most common cause of dementia, the need for more powerful diagnostic tools becomes ever more urgent. A definitive diagnosis of AD is presently obtained by an autopsy that confirms the presence of β -amyloid (A β) peptide plaques and tau protein tangles in brain tissue, but criteria have emerged over the past decade that incorporate molecular imaging and fluid analytes for a differential diagnosis in preclinical stages (Jack et al., 2011; Sperling et al., 2011). Identifying early biomarkers of AD is essential to diagnose and stratify patients for research into effective treatment options, and can aid in the preparation for disease management before debilitating symptoms are present. Magnetic resonance imaging (MRI) is a non-invasive diagnostic technique that can readily detect gross features of brain tissue in order to exclude neurosurgical causes of declining cognition, such as tumor or stroke; mounting evidence indicates its utility in quantifying brain atrophy to assess the severity of AD (see Pini et al, 2017 for review).

It is well established that pathology in AD originates in the region of the hippocampus (Braak and Braak, 1991) and that decreases in the gray matter volume of this region predict the onset of AD (Jack et al., 1999). More recently, parahippocampal white matter volume has also been shown to be a sensitive predictor of AD in cognitively normal people (Stoub et al., 2014). Although hippocampal volumetry is one of the most important imaging MRI biomarkers currently available to assist in AD diagnoses (Teipel et al., 2013), it lacks the specificity to stand alone as an accurate diagnostic test (Frisoni et al., 2010), and indicates an advanced stage of neurodegeneration. Development of MR methods that reveal more subtle microstructural pathologies is an active and promising area of research, because these pathologies might be indicative of progression to AD. Previous studies have demonstrated that certain subregions within the complex internal structure of the hippocampus are differentially implicated in memory function and cognitive impairment (Rössler et al., 2002; West et al., 1994). The application of multiparametric quantitative MRI protocols can provide different types of contrast within the hippocampus (Benveniste et al., 2000; Shepherd et al., 2006; Zhang et al., 2002) and might prove useful to provide specific biomarkers for AD (Maruszak and Thuret, 2014).

Diffusion tensor imaging (DTI) is one such quantitative MRI method (Le Bihan et al., 1986), which has been used extensively to study white matter integrity (Budde et al., 2009, 2007; DeBoy et al., 2007; Song et al., 2002, 2005; Sun et al., 2006). Numerous DTI studies of AD have reported an increased mean diffusivity (MD) and decreased fractional anisotropy (FA) in white matter serving as promising indicators of AD (see Amlien and Fjell, 2014 for review). Given that MD and FA are influenced by water diffusion in both radial and axial planes, the radial (λ_{\perp}) and axial (λ_{\parallel}) diffusivity themselves could give a more precise representation of white matter tissue damage in AD (Song et al., 2004) and may be useful for disease staging by describing different white matter pathologies (Acosta-Cabronero et al., 2012). However, the precise nature of white matter damage in AD has not been characterized, and it remains unknown whether it occurs before or after gray matter damage (Nir et al., 2013). Correlations between DTI changes in gray matter and tissue pathologies are under study, but gray matter diffusivity has been shown to have superior predictive power for AD over conventional volumetry (see Weston et al., 2015 for review).

A growing body of literature has successfully utilized magnetization transfer imaging (MTI) to characterize neurodegenerative disorders including AD (see Tambasco et al., 2015 for review). Several studies have examined the magnetization transfer ratio (MTR) (Wolff and Balaban, 1989), and have found it to decrease in early phases of AD (Ginestroni et al., 2009; Hanyu et al., 2001; Kabani et al., 2002) and map disease progression (Ropele et al., 2012). However, a conflicting finding has been reported in transgenic mouse models of AD, where an increased MTR value appeared to be primarily driven by A β load (Bigot et al., 2014), and even preceded plaque formation and memory deficits (Pérez-Torres et al., 2014). Because the MTR is dependent upon the imaging parameters and field strength chosen by the experimenter, quantitative MTI (qMTI) methods are necessary for an effective comparison between studies. Metrics derived from the two-pool model of magnetization transfer offer more complete information on the macromolecular structures in brain tissue than does the MTR (Henkelman et al., 1993) and several qMTI metrics have been suggested to be useful biomarkers in prodromal stages of AD (Giulietti et al., 2012; Kiefer et al., 2009; Ridha et al., 2007).

In the present study, a single transgenic mouse model of AD is utilized (Tg2576; Hsiao et al., 1996), harboring the Swedish mutation (K670N/M671L) of the gene that codes for human amyloid precursor protein (hAPP695) under the control of mouse prion protein promoter elements. This mutation leads to an abundance of A β in the central nervous system and the formation of A β plaques by 11 to 13 months of age (Hsiao et al., 1996). There appears to be a loss of synapses in the hippocampus and compromised integrity of hippocampal circuitry in animals as young as 4.5 months (Jacobsen et al., 2006; Jung et al., 2011; Lanz et al., 2003). In the absence of tau pathology, this model acts as a powerful reductionist tool for extracting the contribution of amyloid-related pathological changes to the alteration of MR properties.

With a need for understanding and detecting early gray matter changes in AD, this study uses T₁ relaxometry, DTI, and qMTI to study the hippocampus in mice with and without amyloid accumulation. The use of directionally encoded color (DEC) maps from DTI reveals cytoarchitectural details within the hippocampus and allows the identification of cell layers (strata) with characteristic fibre orientations. This produces a richer data set from which to analyze changes in quantitative MR metrics within these otherwise indistinguishable strata. We compare gray matter of the hippocampus and surrounding white matter tracts between the Tg2576 mouse model of AD and control mice using these multiple quantitative MRI metrics and interpret the results based on immunohistochemical staining for A β . To our knowledge, this is the first study to examine qMTI metrics in a mouse model of AD, and the first to examine multiple quantitative MR metrics within the strata of the hippocampus. We aim to determine if the combination of metrics examined in hippocampal strata can provide novel insight into the pathological changes that occur in the hippocampus early in the AD process.

2. Methods

2.1. Mouse model

Six male 7.5 month-old APP_{K670N/M67L} (Hsiao et al., 1996) mice originally obtained from AstraZeneca R&D and derived from B6SJL F1 background were used in this study. Six male 7.5 month-old wild-type mice from the same genetic background served as controls, and allowed for comparative analysis between transgenic and healthy strains. The mice were genotyped by PCR using genomic DNA isolated from tail biopsies at weaning (21 days of age). Unique six-digit numbers were assigned to each mouse and used to identify mice in all experiments so that investigators were blinded to mouse genotype. All mice were provided with food and water *ad libitum* and maintained on a 12-hour light/dark cycle in accordance with the University of Manitoba Animal Care Committees who adhere to the guidelines and principles created by the Canadian Council on Animal Care.

2.2. Euthanasia

All 12 mice were sacrificed for *ex vivo* study at 7.5 months of age. Under deep anesthesia (5% isoflurane in oxygen), the mice were intracardially perfused with 0.1 M phosphate buffered saline (PBS) followed by a fixative solution of 4% paraformaldehyde (PFA). The mouse brains in skulls were removed from the bodies and all external tissue was cleaned off prior to storage in 4% PFA at 4°C. Euthanasia procedures were carried out as per the guidelines and principles of the Canadian Council on Animal Care and were approved by the local Institutional Animal Care Committees at University of Manitoba and University of Winnipeg.

2.3. MRI

Imaging was done on most brains within one month of perfusion with PBS and PFA, with the maximum time spent in PFA being eight weeks. The mouse brains in skulls were transferred to PBS 48 hours before imaging to wash the sample of any fixative. For imaging, the brains in skulls were secured in a custom-built acrylic sample holder and immersed in room temperature Fomblin Perfluoropolyether Y04 grade fluid (Solvay Solexis, Milan, Italy) to maintain hydration, and eliminate external proton signal and susceptibility artifacts. This sample tube was then inserted to a custom-built 24 mm internal diameter, 300 MHz inductively coupled quadrature radiofrequency (RF) volume coil (NRC Institute for Biodiagnostics, Winnipeg, Canada). The coil was loaded inside a Bruker BGA 12-S actively shielded gradient system with integrated shim coils (Bruker BioSpin, Milton, Canada). The experiments were performed on a 7T 21 cm Bruker AVANCE III NMR system running Paravision 5.0 (Bruker BioSpin).

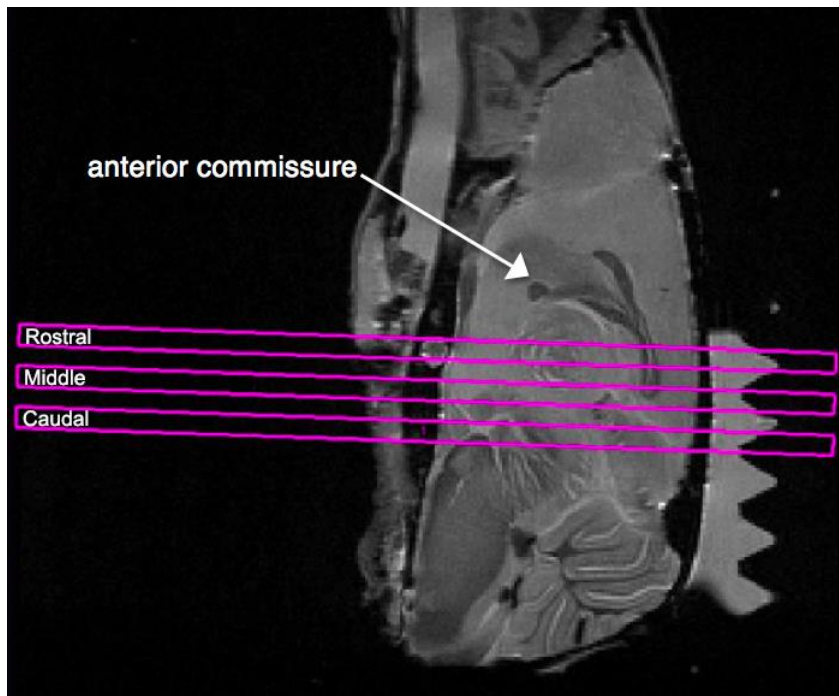


Figure 1. Slice geometry of the coronal slices used for all imaging. The three slices of interest are outlined in magenta and labeled as rostral, middle, and caudal. The middle slice was positioned 2.50 mm caudal to the anterior commissure and had a 0.5 mm slice thickness, with 1.0 mm spacing between slices.

To image the hippocampus and surrounding white matter structures, three coronal slices labeled rostral, middle, and caudal, were selected at a position centered at 2.50 mm caudal to the anterior commissure (Figure 1). The same slice geometry was used for all images to minimize differences in the slice alignment along the rostral-caudal plane when comparing data between mice. Images had a $(2\text{ cm})^2$ field of view and (256×256) matrix size, a 0.5 mm slice thickness, and were spaced with 1.0 mm interslice distance, resulting in images with a $78\ \mu\text{m} \times 78\ \mu\text{m} \times 500\ \mu\text{m}$ resolution.

Relaxation images, DT images, and qMT images were collected during an overnight imaging session for each mouse brain, throughout which time 18°C water-cooled gradients were used to maintain ambient bore temperature.

T_1 data were acquired using a rapid acquisition with refocused echoes (RARE) sequence, with a repetition time (T_R) = (4895.5, 2895.5, 1395.5, 695.5, 295.5, 95.5) ms, effective echo time (T_E) = 11 ms, RARE factor = 2, and 4 averages, for a total experiment time of 71 min.

DTI data were acquired with a pulsed gradient spin echo (PGSE) sequence using a seven-direction tetra-orthogonal gradient-encoding scheme (b -value = $1000\ \text{s}/\text{mm}^2$, gradient pulse duration (δ) = 6 ms, gradient separation time (Δ) = 14 ms, T_E = 26ms, T_R = 5000ms, 6 averages, 8.5 hour experiment time).

MTI data were acquired using one non-saturated and 18 RF-saturated fast low angle shot (FLASH) images (Haase, 1990) (10.25 ms Gaussian saturation pulse with saturation powers of 5, 10, and $20\ \mu\text{T}$ and frequency offsets at each power of 1, 2, 4, 6, 10, and 30 kHz, 32 averages, T_E = 6 ms, T_R = 70 ms, 10° flip angle, 3 hour experiment time).

2.4. Imaging Data Analysis

The potential for small sample movements or drifts in Larmor frequency of the sample during long imaging sessions as well as differences between how spin echo and gradient echo images are spatially encoded due to gradient field inhomogeneities can cause small changes in image alignment. To construct accurate quantitative maps and compare different imaging sequences on a voxel-by-voxel basis, image registration was required (Thiessen et al., 2013). A custom-built MATLAB GUI was used for registration prior to fitting, and all images were aligned to the $b=0$ diffusion-weighted images using a rigid affine transformation matrix determined automatically by maximizing the 2D correlation coefficient in a similar method used before (Thiessen et al., 2013). Furthermore, b -matrices associated with each DWI were rotated to match the registered image orientation (Leemans and Jones, 2009; Thiessen et al., 2013).

An anisotropic diffusion filter was applied before quantitative maps were constructed to improve the signal to noise ratio (Gerig et al., 1992; Perona and Malik, 1990), with five iterations and a gradient modulus threshold equal to three times the standard deviation of the noise in each echo (Jones et al., 2003; Thiessen et al., 2013). A saturation recovery curve was fitted to the data acquired from the RARE images to construct T_1 maps.

Diffusion tensors were determined using a non-linear least squares fit with a modified Cholesky decomposition to ensure positive definiteness (Koay et al., 2006). Diffusion tensor metric maps include mean diffusivity (MD), axial diffusivity (λ_{\parallel}), radial diffusivity (λ_{\perp}), and fractional anisotropy (FA). A DEC map was constructed from the first eigenvector, with bright red pixels representing highly anisotropic diffusion primarily along the x-direction, green along the y-direction, and blue along the z-direction, and isotropic regions appearing gray or brown.

MTIs were normalized to the FLASH image without an MT saturation pulse. These normalized data were fitted to the two-pool model of magnetization transfer (Henkelman et al., 1993) with continuous wave pulse equivalent approximations (Ramani et al., 2002) and a super-Lorentzian absorption lineshape for the bound pool (Thiessen et al., 2013). qMTI metric maps were made including the magnetization transfer rate from the bound to liquid pools (RM_0^A), longitudinal relaxation rate of the free pool (R_A), transverse relaxation times of the free and bound pools (T_2^A and T_2^B), and the bound pool fraction (f). The longitudinal relaxation rate of the bound pool (R_B) was fixed arbitrarily to $1/s$ as recommended by several groups (Henkelman et al., 1993; Ramani et al., 2002). R_A was estimated using the T_1 map (Henkelman et al., 1993; Ramani et al., 2002). Using the fitted value of $f/R_A(1-f)$, the bound pool fraction can be calculated using R_A .

Using a custom-built MATLAB program, regions of interests (ROIs) were selected in the DEC map with reference to a mouse atlas (Paxinos and Franklin, 2001) and applied to analysis of all registered quantitative MR maps (Figure 2). The segmentation was performed by a single rater, and the intra-rater reliability was assessed by multiple rounds of segmentation on the same images. The output from these repeated segmentations was compared to ensure consistency in tracing ROIs both within and between samples. While some groups have demonstrated success with automated segmentation of the murine hippocampus (Ali et al., 2005; Lau et al., 2008; Scheenstra et al., 2009), our previous study (Hayes et al., 2014) found that automated segmentation was not as reliable as manual segmentation due to poorer contrast at the boundaries of this small structure.

The first ROI to be outlined was the whole hippocampus, comprised of the hippocampus proper with the adjacent dentate gyrus. A second set of ROIs defined individual strata within the molecular cell layer of the hippocampus, namely the stratum radiatum (H_{rad}) and stratum lacunosum moleculare (H_{lm}), and the two regions of the molecular layer of the dentate gyrus (designated DG_{mt} and DG_{mb} for top and bottom, respectively) that surround the granule and polymorph layers of the dentate gyrus (DG_{gp}). Of the surrounding white matter, selected ROIs were the cingulum (cg), corpus callosum (cc), fimbria of the hippocampus (fi), external capsule (ec), brachium of the superior colliculus (bsc), and dorsal hippocampal commissure (dhc).

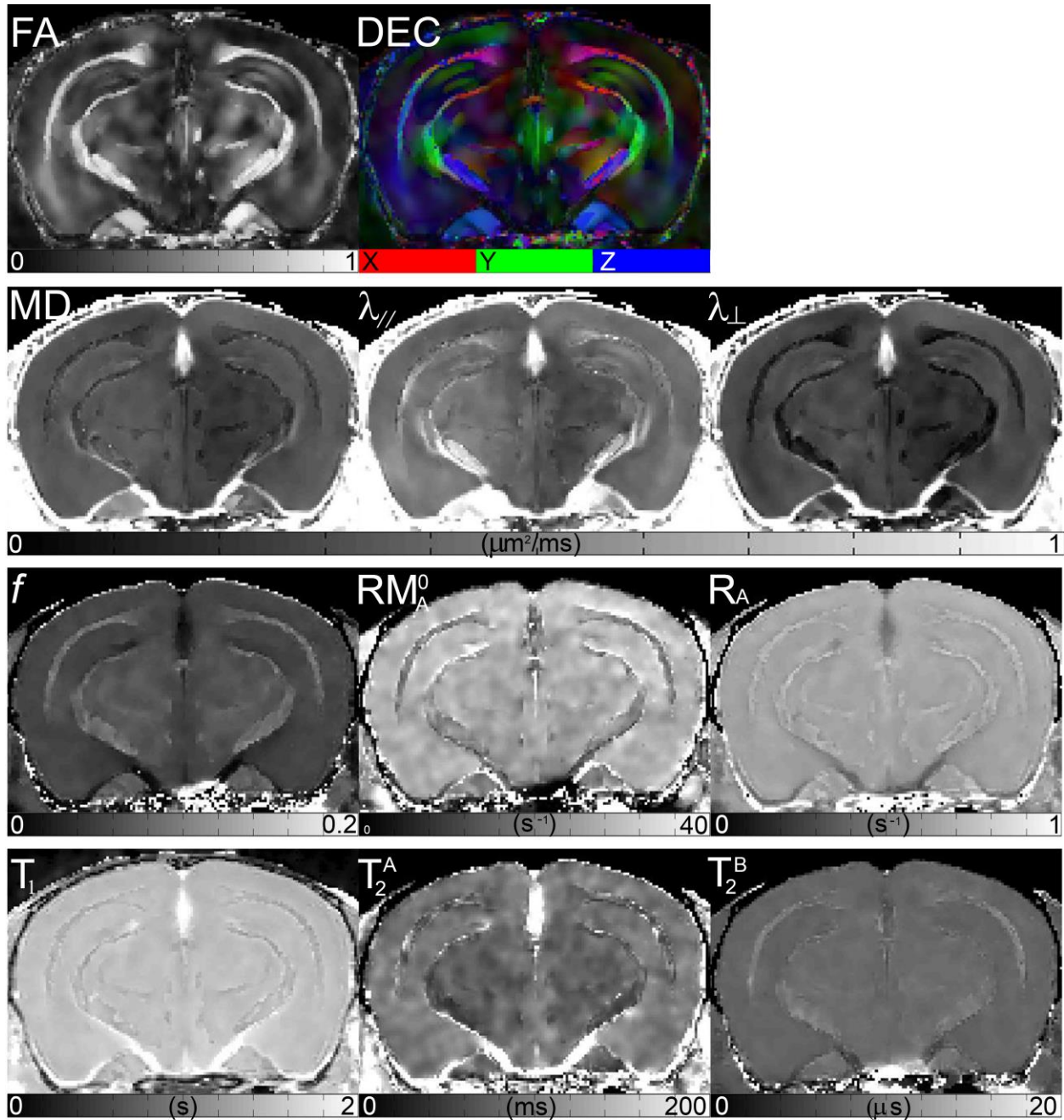


Figure 2. Quantitative MRI maps of the middle slice of a representative Tg2576 mouse brain. The scale from black to white is given below each map. Various white matter tracts are visible with varying contrast in all of the different quantitative MRI maps, but cell layers within the gray matter of the hippocampus proper and dentate gyrus are only visible in FA and DEC maps. **Maps:** fractional anisotropy (FA), directionally encoded color (DEC), mean diffusivity (MD), axial diffusivity (λ_{\parallel}), radial diffusivity (λ_{\perp}), bound pool fraction (f), magnetization transfer rate from the bound to liquid pools (RM_A^0), longitudinal relaxation rate of the free pool (R_A), spin-lattice relaxation time (T_1), and transverse relaxation times of the free and bound pools (T_2^A and T_2^B).

2.5. Immunohistochemistry

Following imaging, the fixed brains were dissected from skulls and a coronal section encompassing the imaged slices was then placed in a plastic cassette and transferred to an Automated Vacuum Tissue Processor (ASP300S; Leica, Wetzlar, Germany), which processed the samples overnight through the following programme: formalin Hold step (until the programme is ready to run); 70% ethanol (1 hour); 90% ethanol (1 hour); 100% ethanol x 4 (1 hour per ethanol); xylene x 3 (1 hour per xylene); molten wax x 3 (1 hour per wax change). Once processing was complete, the samples were transferred to the wax bath of the Tissue Embedding Station (Leica EG1150H). The samples were then embedded in fresh molten paraffin wax and solidified using the Leica G1150C cooling unit.

The wax blocks were mounted to a Leica RM2135 rotary microtome, which was used to trim the block face until a position of 1.5 mm posterior to the anterior commissure of the brain was reached, corresponding to the level of the rostral imaging slice (See Figure 1). The blocks were cooled and rehydrated before 4µm sections were cut, floated out on a warm (42°C) water bath, then mounted in series on Superfrost Plus slides (Thermo Fisher Scientific, Waltham, USA). This process was repeated at the middle and caudal levels of the hippocampus, so that each slide held three sections that were about 1 mm apart. The slides were air dried at room temperature in racks for a minimum of one hour and then in a 40°C heating chamber overnight. The sections were de-waxed in xylene and rehydrated through a series of alcohols, decreasing in concentration to water.

Immunohistochemical staining for A β plaques was conducted using a Ventana XT automated staining machine (Ventana Medical Systems, Oro Valley, USA) at room temperature as per an optimised protocol and manufacture specific reagents. Pre-treatment consisted of 98% formic acid for 8 minutes then a wash with Ventana Reaction Buffer, followed by washing in cold running water for 5 minutes. The samples were then wet-loaded in Reaction Buffer onto the Ventana XT, which applied a CC1 heat pre-treatment for 30 minutes in an EDTA Boric Acid Buffer (pH 9.0) before being blocked for 8 minutes using Superblock (#88-4101-00; Mediate, Chicago, USA). The primary antibody against A β (82E1, 0.2µg/ml; IBL, Hamburg, Germany), a biotinylated mouse monoclonal antibody, was directly applied to each slide without a wash step. After 8 hours of antibody incubation, the Ventana XT applied tertiary reagent DABMap (Ventana), then the 3,3'-diaminobenzidine (DAB) substrate followed by a haematoxylin counterstain for 4 minutes and a Blueing agent (Ventana) for 4 minutes.

The slides were removed from the staining machine, washed in soapy water for 5 minutes, rinsed in distilled water, then placed in an Automated Slide Stainer (Gemini AS, Thermo Fisher Scientific) for dehydration through an alcohol series, clearance in xylene, and permanent mounting with DPX mountant. Imaging was done using a Leica DM1000 microscope and Leica Application Suite V4.8, and images of each section were analysed to determine the burden of amyloid pathology.

2.6. Statistical analysis

The various MRI metrics were compared statistically between the mouse genotypes using a one-way analysis of variance (ANOVA). All analyses were conducted in IBM SPSS Statistics Version 19.0 (IBM Corp., Armonk, NY, 2010). Statistical significance was predetermined at $p < 0.05$.

3. Results

Example maps of various quantitative MRI metrics are presented in Figure 2. Note that the hippocampus has little visual contrast in the qMTI and relaxation maps, and all DTI maps other than the DEC and FA maps. The boundaries between different hippocampal strata and white matter tracts are especially apparent in the DEC map, which was used to trace all ROIs as shown in Figure 3. Note that all ROIs appear in both left and right hemispheres but are labelled in Figure 3 only on the left. The mean value of all metrics presented below, and summarized in Tables A1 through A3, is the spatial average of both the left and right for all ROIs except the corpus callosum, which spans the midline.

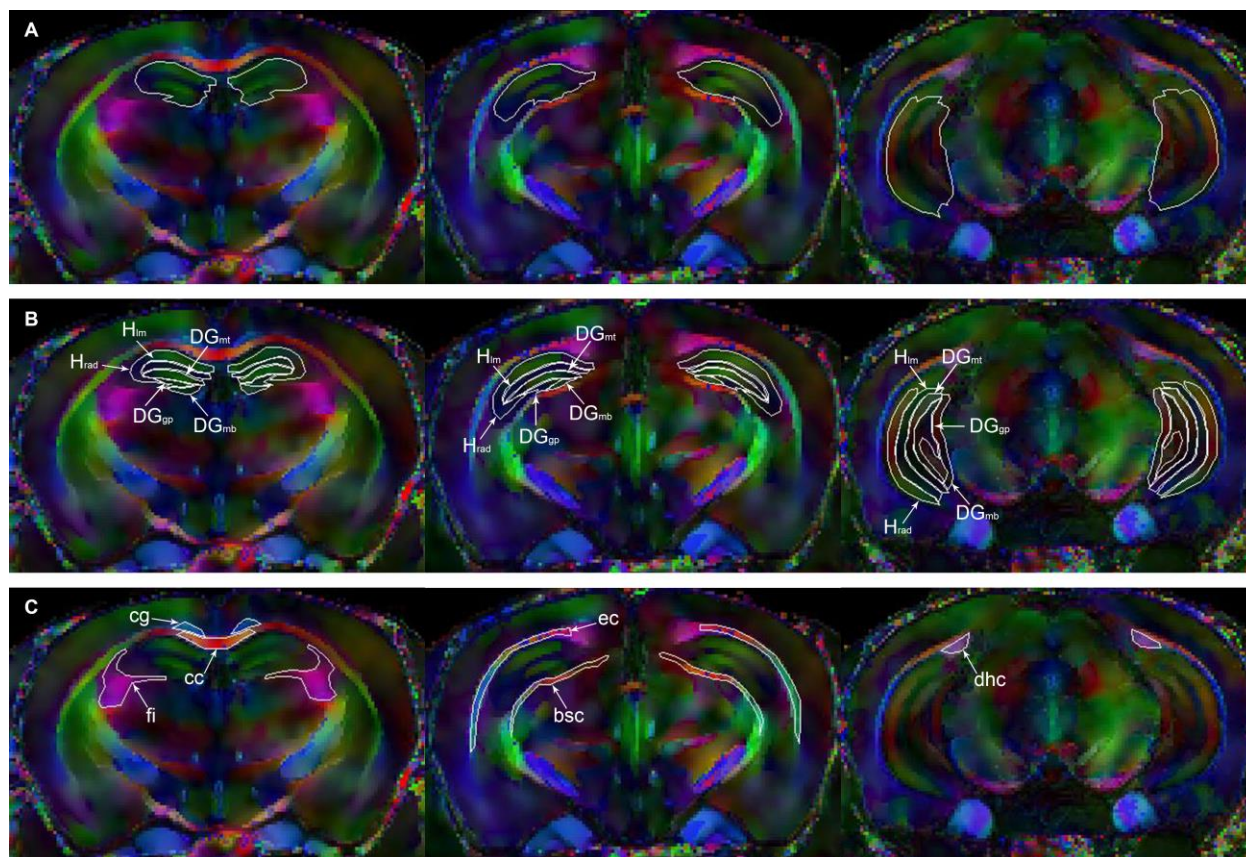


Figure 3. DEC maps of a representative Tg2576 mouse brain from each of the three slices. The red, green, and blue colours each represent the x-, y-, and z- directions of water diffusion respectively, and the brightness of the pixels corresponds to anisotropy. The entire hippocampus proper and dentate gyrus are outlined together in white in (A). Hippocampal strata ROIs are outlined in white and indicated by arrows in (B), and white matter ROIs are similarly labelled in (C). Note that all ROIs appear in both left and right hemispheres but are labelled here only on the left. The mean value of all metrics calculated is the spatial average of both the left and right for all ROIs except the corpus callosum, which spans the midline. **ROIs: Hippocampal:** radiatum (H_{rad}) and lacunosum-moleculare (H_{lm}) layers of the hippocampus; top/bottom molecular (DG_{mt}/DG_{mb}) and granular/polymorph (DG_{gp}) layers of the dentate gyrus. **White matter:** cingulum (cg), corpus callosum (cc), fimbria of the hippocampus (fi), external capsule (ec), brachium of the superior colliculus (bsc), and dorsal hippocampal commissure (dhc).

3.1. Hippocampus

When the entire hippocampus was segmented as a uniform ROI, there were fewer statistically significant differences in multiple metrics between transgenic mice and controls, than was seen when analyzing hippocampal cell layers. This multiparametric variance is illustrated in Figure 4, where DEC maps are shown in grayscale to highlight regions with two or more significant differences. Only the middle section of the whole hippocampus was found to have differences in T_1 and FA values between groups (Figure 4A). However, when comparing the specific strata, metrics that did not differ significantly in the whole hippocampus displayed several significant differences, while the FA and T_1 values did not differ consistently across all ROIs (Figure 4B).

Specifically, segmentation of the whole hippocampus indicated that the T_1 values of Tg2576 mice were significantly lower than those of control mice only in the middle section (1.53 ± 0.07 s control, 1.40 ± 0.10 s APP), while the FA was higher within all sections (rostral 0.15 ± 0.02 control, 0.29 ± 0.04 APP; middle 0.16 ± 0.03 control, 0.23 ± 0.03 APP; caudal 0.21 ± 0.03 control, 0.25 ± 0.04 APP) (Table A1). Examining the T_1 and FA values in hippocampal strata revealed that the DG_{mt} was the only cell layer that contained significant differences in both metrics across all sections (T_1 : rostral 1.47 ± 0.07 s control, 1.38 ± 0.05 s APP; middle 1.51 ± 0.06 s control, 1.40 ± 0.01 s APP; caudal 1.47 ± 0.06 s control, 1.40 ± 0.06 s APP. FA: rostral 0.13 ± 0.03 control, 0.18 ± 0.05 APP; middle 0.15 ± 0.04 control, 0.22 ± 0.04 APP; caudal 0.16 ± 0.02 control, 0.22 ± 0.04 APP). The H_{lm} in the middle section was also altered in both T_1 (1.56 ± 0.05 s control, 1.40 ± 0.01 s APP) and FA (0.15 ± 0.03 control, 0.21 ± 0.04 APP). No significant differences between groups were found in other DTI metrics (MD, λ_{\perp} , or λ_{\parallel}) in any areas of the hippocampus.

The qMTI-derived R_A was not significantly altered in transgenic versus control mice in the whole hippocampus. However, when the hippocampus was segmented into strata it was apparent that the mice did exhibit significantly greater R_A values within all strata but the DG_{gp} . When combined with the altered T_1 and FA values in various strata, three regions emerged as significant for differences in all three metrics: the rostral DG_{mt} (R_A : 0.66 ± 0.04 s⁻¹ control, 0.71 ± 0.03 s⁻¹ APP), middle H_{lm} (R_A : 0.62 ± 0.02 s⁻¹ control, 0.69 ± 0.06 s⁻¹ APP), and caudal DG_{mt} (R_A : 0.65 ± 0.03 s⁻¹ control, 0.70 ± 0.03 s⁻¹ APP). The f and T_2^A values were also significantly changed in Tg2576 mice relative to controls in the caudal section of the hippocampus, while RM_0^A and T_2^B did not appear changed by expression of the APP transgene.

3.2. White matter

In white matter, the regions with significantly decreased T_1 relaxation times and increased FA values in Tg2576 mice compared to controls were the cingulum (T_1 : 1.41 ± 0.05 s control, 1.34 ± 0.05 s APP; FA: 0.48 ± 0.06 control, 0.59 ± 0.05 APP) and the dorsal hippocampal commissure (T_1 : 1.48 ± 0.05 s control, 1.38 ± 0.05 s APP; FA: 0.59 ± 0.07 control, 0.69 ± 0.05 APP). These regions were also significantly different in R_A values (cg: 26.7 ± 4.8 s⁻¹ control, 23.3 ± 5.0 s⁻¹ APP; dhc: 25.6 ± 4.9 s⁻¹ control, 26.5 ± 5.5 s⁻¹ APP).

As in the hippocampus, no significant differences were observed in the MD or $\lambda_{//}$ values of white matter regions. The only statistically significant change in T_2^B in white matter was also in the cingulum, where Tg2576 mice had values higher than control mice. RM_0^A and T_2^A did not show any significant differences in any white matter region.

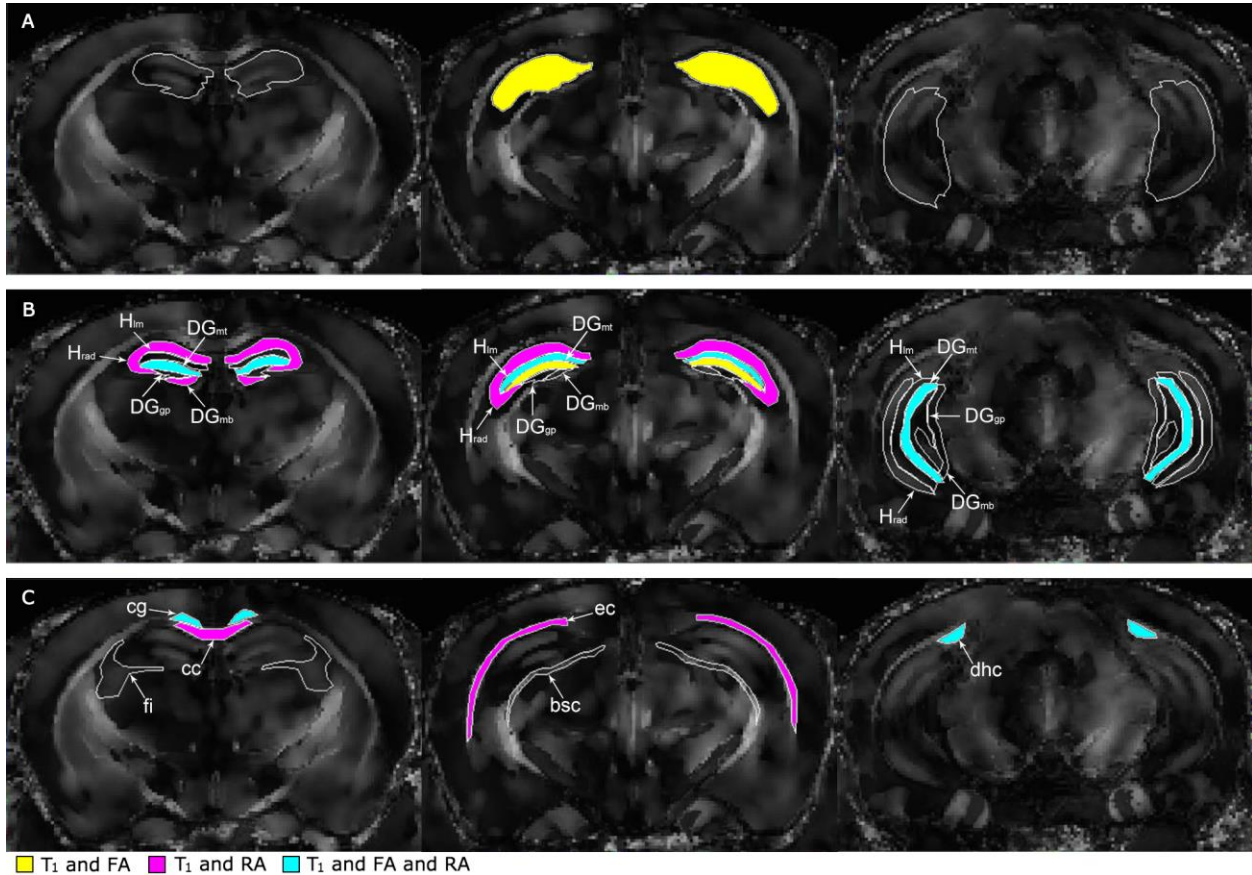


Figure 4. Unsaturated DEC maps of a representative Tg2576 mouse brain with regions of interest coloured-in to indicate statistically significant difference between transgenic and control mice in multiple metrics. Results are presented from the whole hippocampal region (A), each hippocampal cell layer (B), and white matter regions (C). Hippocampal cell layers (B) appear in each of the rostral (leftmost), middle, and caudal (rightmost) slices, whereas the white matter regions (C) appear in only one slice. All regions are outlined in white and are filled in if they contain significant group differences in T_1 and FA (yellow), T_1 and R_A (magenta), or a combination of T_1 , FA and R_A (cyan). ($p < 0.05$ using a one-way ANOVA).

3.3. Histology

To confirm that the mice in this study did exhibit pathological $A\beta$ deposition, regions of interest were probed for intracellular amyloid and $A\beta$ plaque load by immunohistochemical techniques (82E1 antibody). Light microscopy revealed a low degree of $A\beta$ pathology in the hippocampus of Tg2576 mice whereas there was no $A\beta$ detected in the brains of control mice. In transgenic animals, the hippocampal $A\beta$ was visible as a 1-3 diffuse plaques in each section (Figure 5A,B,D, arrows). The anti- $A\beta$ antibody, though capable of binding to soluble $A\beta$ as well as extracellular plaques, did not reveal any intracellular $A\beta$ accumulation.

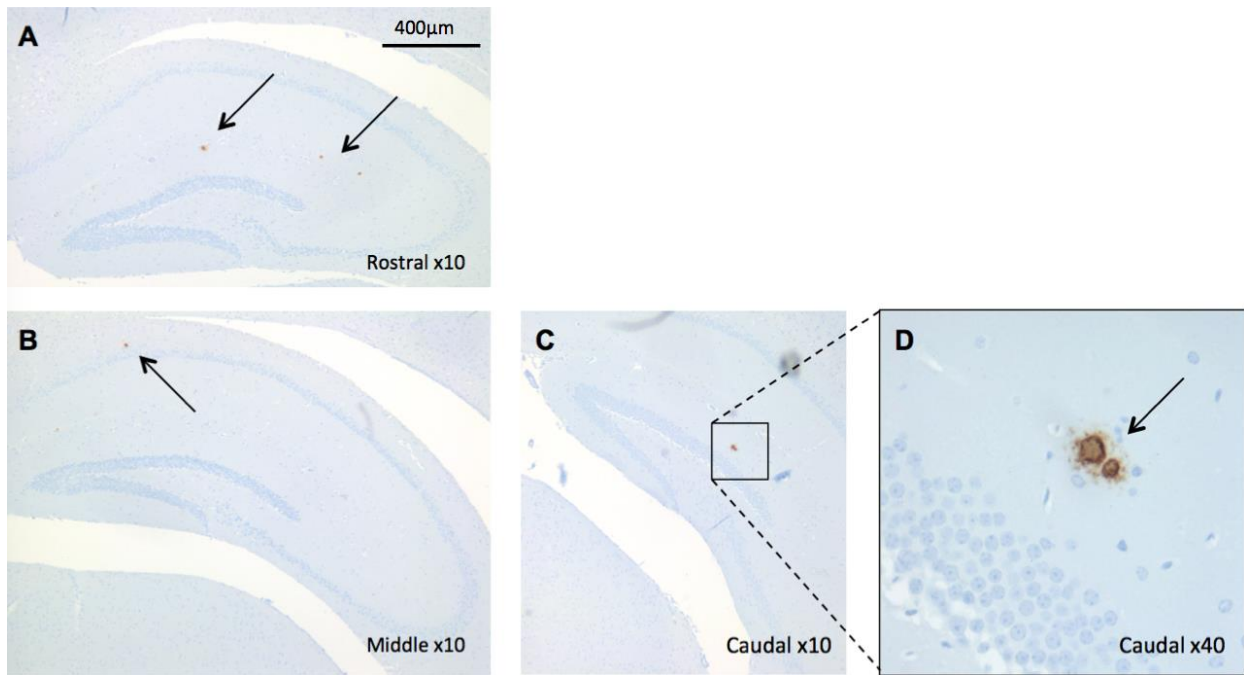


Figure 5. Immunohistochemical staining for A β in a representative 7.5-month-old Tg2576 mouse hippocampus, at rostral (**A**), middle (**B**), and caudal (**C**) levels. A β deposition (brown) as detected by anti-A β antibody 82E1, was evident as extracellular plaques (indicated by arrows) in the hippocampal and dentate gyrus cell layers. Intracellular staining for A β was not apparent, and the plaques appeared diffuse upon magnification (**D**).

4. Discussion

While the FA map provided high contrast between white and gray matter as well as moderate contrast between hippocampal strata, the DEC map was the most informative for segmentation purposes. The DEC map was beneficial in revealing the fibre orientations of white and gray matter structures, thereby removing ambiguity in the borders between neighbouring ROIs. The identification of these individual strata in our three slices offers considerably more information on changes in relaxometry, DTI, and qMTI metrics between and within groups of mice, relative to the analysis of the hippocampus as a homogeneous gray matter structure. This highlights the complexity and variation of pathology within the hippocampus, and warrants more comprehensive coverage of the entire hippocampal length.

We chose a fixed number of slices with the same resolution to accommodate the limitations of each MRI sequence and improve registration between images. Specifically, both the DTI and T₁ mapping sequences use a 2D spin echo sequence, which limits the number of slices in a given repetition time. Furthermore, the qMTI method requires multiple GRE acquisitions and is sensitive to magnetization transfer effects that can arise from RF pulses used in multislice acquisitions. In our study, 2D slicing of the hippocampus facilitated comparison between DTI and qMTI metrics. Additional 2D slices or a 3D acquisition across all of the imaging sequences would have increased experiment time and introduced confounding effects in the qMTI model. Significant differences between groups of mice were found to vary across our three slices in several DTI and qMTI metrics, which could be focused on to reduce total imaging time in future 3D imaging studies of the hippocampus. Such studies could relate the quantitative MR results to the regional spread of tissue pathologies over time.

Our histological investigation of the brain tissue validated the Tg2576 mice as models of A β deposition, and also established that at 7.5 months of age there was a less severe degree of pathology than at 11-13 months (Hsaio et al., 1996), which could correspond to an earlier disease stage. Indeed, Tg2576 mice are generally asymptomatic in terms of most behavioural tests at 7.5 months of age, but have exhibited impaired hippocampal learning in contextual fear conditioning by 5 months of age, several months prior to detection of A β plaques (Jacobsen et al., 2006). Therefore, other cellular changes indicative of early AD pathology, such as astrogliosis, may be more relevant in mice at this age. Preparation of our mouse brain tissue precluded an electron microscopic examination, which might have shown more subtle changes in ideally processed tissue. The brains used in this study were fixed with PFA rather than glutaraldehyde, and consequently electron microscopy studies were unsuitable. Therefore, interpretation of the precise mechanisms that account for the MR findings must also be informed by the literature about the pathological characteristics of our transgenic mouse model at the age of 7.5 months.

The earliest documented histopathological feature of Tg2576 mice is the loss of dendritic spines in the hippocampal regions at 4.5 months of age (Lanz et al., 2003). However, they are also known to have higher than normal concentrations of soluble A β peptides within their brains as they age (Duff et al., 1996; Hsiao et al., 1996). It is hypothesized that these peptides are prone to aggregate into oligomers, which form upstream of plaques and may be the toxic species in Alzheimer's disease that trigger synaptic alterations and induce memory deficits (Cleary et al., 2005; Hardy, 2009; Lambert et al., 1998; Walsh et al., 2002). In our study, the sparse distribution

of plaques prevented their quantification and correlation with altered MR metrics. Longitudinal studies that compare the accumulation of A β oligomers in this mouse model would be more informative as to the relationship between the molecular pathogenic processes, and the altered tissue properties and water movement underlying our multiparametric MRI changes.

Our results were consistent with another study that found significant reductions in T_1 at 4.7 T, which correlated with A β stain intensity in both white matter and hippocampal gray matter regions of an 5xTg mouse model of AD (Spencer et al. 2013). Decreased T_2 relaxation times have been measured in cortical and hippocampal regions of plaque-bearing AD mouse models, and even in the brains of mice preceding plaque formation (Falangola et al., 2007). Because the deficits and anatomical differences vary considerably among AD mouse models depending on the particular gene mutation, promoter element, and background strain of mouse used, it is important for reliable imaging techniques to be able to detect and quantify microstructural changes within the hippocampal strata. Further studies are needed with full electron microscopy characterization of the tissue to determine the precise reason for the proton relaxation time changes observed in this study, and the additional DTI and qMTI metrics might shed light upon changes in water mobility and exchange within and between the free water and macromolecular tissue compartments.

This study builds upon previous investigations into the gray matter pathology of AD mouse models and the meaning of DTI and qMTI measurements in healthy and diseased white matter (Duff et al., 1996; Hsiao et al., 1996; Thiessen et al., 2013). In doing so it also highlights two complementary knowledge gaps, one being the nature of white matter damage in AD mouse models and the other being the histopathological correlates of these quantitative MR metrics in gray matter. Comparison of the results from both white matter and hippocampal gray matter regions are useful in elucidating some of the potential mechanisms of change in these metrics. The white matter regions selected, except for the brachium of the superior colliculus, are all projections of the limbic system and carry highly relevant information for cognitive performance in directionally coherent pathways. In contrast, the neuronal circuits in the hippocampus are significantly smaller and more heterogeneous than these white matter fibre bundles, often containing two or more crossing fibre pathways that could reduce the apparent anisotropy. Nonetheless, the DT protocols employed in this study were capable of detecting similar significant alterations in anisotropy and diffusivity within both white and gray matter ROIs, which demonstrates their applicability in gray matter. Eigenvalues of diffusivity did not indicate robust differences between our mice in either white or gray matter. Several groups have observed changes in eigenvalue measurements in white and gray matter, but only in transgenic mice older than 8 months of age (Harms et al., 2006; Song et al., 2004; Sun et al., 2014).

A previous study has shown that in white matter, f is the most specific qMTI measurement of demyelination (Thiessen et al., 2013). In this study, while f varied between mice in caudal gray matter regions, we detected no significant differences in f between mice in any white matter structures. Bigot et al. (2014) similarly reported no decrease in the MTR in white matter between AD transgenic and control mice, coinciding with no alterations in myelin content as determined from immunofluorescent analysis. These findings reinforce those by Kastyak-Ibrahim et al. (2013), in which a triple transgenic mouse model of AD showed no white matter changes in quantitative MRI or histological staining for myelin. This leads to the

suspicion that myelin damage is not the primary driving force behind the decrease in f that we saw within the caudal sections of the hippocampus in our Tg2576 mice. Although the cause of this change cannot be conclusively determined without the support of histopathological evidence, our results imply that qMTI metrics are sensitive to more complex changes in gray matter than could be explained by myelin loss. We chose to highlight R_A changes in Figure 4, because despite being derived in part from T_1 , R_A is not completely interdependent with T_1 (see Figure 4, yellow ROIs) and can in fact provide additional information from the two-pool model.

The analyses carried out in our study were with high resolution images and in fixed brains whereas many previous findings used live mice with images of less contrast to define ROIs. There are differences in some MR metrics when imaging chemically fixed *ex vivo* samples as opposed to *in vivo* samples. Certain tissue properties are altered by the action of formaldehyde fixative, namely protein cross-linking, dehydration, tissue degradation, and decreased fibre length (Shepherd et al., 2009). Sun et al. (2009, 2005) demonstrated that diffusion anisotropy is relatively unaffected by fixation, while Schmierer et al. (2008) described significant differences in the *ex vivo* and *in vivo* values of several other diffusivity (MD, λ_{\parallel} , λ_{\perp}), relaxation, and magnetization transfer (f , RM_0^A) metrics. Zhang et al. (2012) found that in a mouse model of demyelination, *ex vivo* λ_{\perp} is a more sensitive indicator of myelin than *in vivo* λ_{\perp} . For the purposes of this study, the advantages of *ex vivo* imaging compensate for the challenges of a direct comparison between *ex vivo* and *in vivo* measurements. *Ex vivo* images are of superior quality because they are devoid of any motion artifacts, and the long scan times permit both higher signal-to-noise ratios in the images and the acquisition of a wide array of MR metrics from which to identify the most robust indicators of change and provide a direction for further investigation.

5. Conclusions

This work demonstrates that a combination of quantitative MRI methods can provide valuable information on AD pathology within the murine hippocampus. Directionally encoded color maps are useful to identify the cell layers within the hippocampus and present the possibility of detecting regional differences in a set of T_1 , DTI, and qMTI metrics that were not detected in the hippocampus as a whole. Further studies are necessary to correlate these MRI findings with electron microscopy of the brain tissue. This work is the first step toward longitudinal *in vivo* studies for tracking disease progression and testing therapeutic treatments.

Acknowledgements

This work was supported by the Natural Sciences and Engineering Research Council of Canada (NSERC), Research Manitoba, Canada Foundation for Innovation, and Manitoba Research and Innovation Fund. Additionally, we thank the NSERC Chair for Women in Science and Engineering (Prairies) for providing the ICAN-WISE Scholarship that funded the initial collaboration between H. Whittaker and M. Martin. We would like to thank Marc Del Bigio for histological consultation, and Sheryl Herrera and Vanessa Palmer for assistance with MATLAB analysis.

Disclosure Statement

The authors have no conflicts of interest to declare.

References

- Acosta-Cabronero, J., Alley, S., Williams, G.B., Pengas, G., Nestor, P.J., 2012. Diffusion tensor metrics as biomarkers in Alzheimer's disease. *PLoS One* 7, e49072. doi:10.1371/journal.pone.0049072
- Ali, A.A., Dale, A.M., Badaea, A., Johnson, G.A., 2005. Automated segmentation of neuroanatomical structures in multispectral MR microscopy of the mouse brain. *Neuroimage* 27, 425–435. doi:10.1016/j.neuroimage.2005.04.017
- Amlien, I.K., Fjell, A.M., 2014. Diffusion tensor imaging of white matter degeneration in Alzheimer's disease and mild cognitive impairment. *Neuroscience*. 276, 206-15. doi:10.1016/j.neuroscience.2014.02.017
- Benveniste, H., Kim, K., Zhang, L., Johnson, G.A., 2000. Magnetic resonance microscopy of the C57BL mouse brain. *Neuroimage* 11, 601–11. doi:10.1006/nimg.2000.0567
- Bigot, C., Vanhoutte, G., Verhoye, M., Van der Linden, A., 2014. Magnetization transfer contrast imaging reveals amyloid pathology in Alzheimer's disease transgenic mice. *Neuroimage* 87, 111–119. doi:10.1016/j.neuroimage.2013.10.056
- Braak, H., Braak, E., 1991. Neuropathological staging of Alzheimer-related changes. *Acta Neuropathol.* 82, 239–259. doi:10.1007/BF00308809
- Budde, M.D., Kim, J.H., Liang, H.-F., Schmidt, R.E., Russell, J.H., Cross, A.H., Song, S.-K., 2007. Toward accurate diagnosis of white matter pathology using diffusion tensor imaging. *Magn. Reson. Med.* 57, 688–695. doi:10.1002/mrm.21200
- Budde, M.D., Xie, M., Cross, A.H., Song, S.-K., 2009. Axial diffusivity is the primary correlate of axonal injury in the experimental autoimmune encephalomyelitis spinal cord: a quantitative pixelwise analysis. *J. Neurosci.* 29, 2805–2813. doi:10.1523/JNEUROSCI.4605-08.2009
- Cleary, J.P., Walsh, D.M., Hofmeister, J.J., Shankar, G.M., Kuskowski, M.A., Selkoe, D.J., Ashe, K.H., 2005. Natural oligomers of the amyloid-beta protein specifically disrupt cognitive function. *Nat. Neurosci.* 8, 79–84. doi:10.1038/nn1372

- DeBoy, C.A., Zhang, J., Dike, S., Shats, I., Jones, M., Reich, D.S., Mori, S., Nguyen, T., Rothstein, B., Miller, R.H., Griffin, J.T., Kerr, D.A., Calabresi, P.A., 2007. High resolution diffusion tensor imaging of axonal damage in focal inflammatory and demyelinating lesions in rat spinal cord. *Brain* 130, 2199–2210. doi:10.1093/brain/awm122
- Duff, K., Eckman, C., Zehr, C., Yu, X., Prada, C.M., Perez-tur, J., Hutton, M., Buee, L., Harigaya, Y., Yager, D., Morgan, D., Gordon, M.N., Holcomb, L., Refolo, L., Zenk, B., Hardy, J., Younkin, S., 1996. Increased amyloid-beta₄₂(43) in brains of mice expressing mutant presenilin 1. *Nature* 383, 710–713. doi:10.1038/383710a0
- Falangola, M.F., Dyakin, V. V., Lee, S.P., Bogart, A., Babb, J.S., Duff, K., Nixon, R., Helpern, J.A., 2007. Quantitative MRI reveals aging-associated T2 changes in mouse models of Alzheimer's disease. *NMR Biomed.* 20, 343–351. doi:10.1002/nbm.1163
- Frisoni, G.B., Fox, N.C., Jack, C.R., Scheltens, P., Thompson, P.M., 2010. The clinical use of structural MRI in Alzheimer disease. *Nat. Rev. Neurol.* 6, 67–77. doi:10.1038/nrneurol.2009.215
- Gerig, G., Kubler, O., Kikinis, R., Jolesz, F.A., 1992. Nonlinear anisotropic filtering of MRI data. *IEEE Trans. Med. Imaging* 11, 221–232. doi:10.1109/42.141646
- Ginestroni, A., Battaglini, M., Della Nave, R., Moretti, M., Tessa, C., Giannelli, M., Caffarra, P., Nacmias, B., Bessi, V., Sorbi, S., Bracco, L., De Stefano, N., Mascalchi, M., 2009. Early structural changes in individuals at risk of familial Alzheimer's disease: A volumetry and magnetization transfer MR imaging study. *J. Neurol.* 256, 925–932. doi:10.1007/s00415-009-5044-3
- Giulietti, G., Bozzali, M., Figura, V., Spanò, B., Perri, R., Marra, C., Lacidogna, G., Giubilei, F., Caltagirone, C., Cercignani, M., 2012. Quantitative magnetization transfer provides information complementary to grey matter atrophy in Alzheimer's disease brains. *Neuroimage* 59, 1114–1122. doi:10.1016/j.neuroimage.2011.09.043
- Haase, A., 1990. Snapshot FLASH MRI. Applications to T1, T2, and chemical-shift imaging. *Magn. Reson. Med.* 13, 77–89. doi:10.1002/mrm.1910130109
- Hanyu, H., Asano, T., Sakurai, H., Takasaki, M., Shindo, H., Abe, K., 2001. Magnetization transfer measurements of the hippocampus in the early diagnosis of Alzheimer's disease. *J. Neurol. Sci.* 188, 79–84. doi:10.1016/S0022-510X(01)00553-6
- Hardy, J., 2009. The amyloid hypothesis for Alzheimer's disease: A critical reappraisal. *J. Neurochem.* doi:10.1111/j.1471-4159.2009.06181.x
- Harms, M.P., Kotyk, J.J., Merchant, K.M., 2006. Evaluation of white matter integrity in ex vivo brains of amyloid plaque-bearing APP^{sw} transgenic mice using magnetic resonance diffusion tensor imaging. *Exp. Neurol.* 199, 408–415. doi:10.1016/j.expneurol.2006.01.002
- Hayes, K., Buist, R., Vincent, T.J., Thiessen, J.D., Zhang, Y., Zhang, H., Wang, J., Summers, A.R., Kong, J., Li, X.M., Martin, M., 2014. Comparison of manual and semi-automated segmentation methods to evaluate hippocampus volume in APP and PS1 transgenic mice obtained via in vivo magnetic resonance imaging. *J. Neurosci. Methods* 221, 103–111. doi:10.1016/j.jneumeth.2013.09.014

- Henkelman, R.M., Huang, X., Xiang, Q.S., Stanisz, G.J., Swanson, S.D., Bronskill, M.J., 1993. Quantitative interpretation of magnetization transfer. *Magn. Reson. Med.* 29, 759–766. doi:10.1002/mrm.1910290607
- Hsiao, K., Chapman, P., Nilsen, S., Eckman, C., Harigaya, Y., Younkin, S., Yang, F., Cole, G., 1996. Correlative memory deficits, Abeta elevation, and amyloid plaques in transgenic mice. *Science* 274, 99–102. doi:10.1126/science.274.5284.99
- Jack, C.R., Albert, M., Knopman, D.S., McKhann, G.M., Sperling, R.A., Carrillo, M.C., Thies, B., Phelps, C.H., 2011. Introduction to revised criteria for the diagnosis of Alzheimer's disease: National Institute on Aging and the Alzheimer's Association workgroup. *Alzheimer's Dement.* 7, 257–262. doi:10.1016/j.jalz.2011.03.004
- Jack, C.R., Petersen, R.C., Xu, Y.C., O'Brien, P.C., Smith, G.E., Ivnik, R.J., Boeve, B.F., Waring, S.C., Tangalos, E.G., Kokmen, E., 1999. Prediction of AD with MRI-based hippocampal volume in mild cognitive impairment. *Neurology* 52, 1397–1403. doi:10.1212/WNL.52.7.1397
- Jacobsen, J.S., Wu, C.-C., Redwine, J.M., Comery, T.A., Arias, R., Bowlby, M., Martone, R., Morrison, J.H., Pangalos, M.N., Reinhart, P.H., Bloom, F.E., 2006. Early-onset behavioral and synaptic deficits in a mouse model of Alzheimer's disease. *Proc. Natl. Acad. Sci. U. S. A.* 103, 5161–5166. doi:10.1073/pnas.0600948103
- Jones, C.K., Whittall, K.P., MacKay, A.L., 2003. Robust myelin water quantification: Averaging vs. spatial filtering. *Magn. Reson. Med.* 50, 206–209. doi:10.1002/mrm.10492
- Jung, J.H., An, K., Kwon, O. Bin, Kim, H.S., Kim, J.H., 2011. Pathway-specific alteration of synaptic plasticity in Tg2576 mice. *Mol. Cells* 32, 197–201. doi:10.1007/s10059-011-0077-8
- Kabani, N.J., Sled, J.G., Chertkow, H., 2002. Magnetization transfer ratio in mild cognitive impairment and dementia of Alzheimer's type. *Neuroimage* 15, 604–610. doi:10.1006/nimg.2001.0992
- Kastyak-Ibrahim, M.Z., Di Curzio, D.L., Buist, R., Herrera, S.L., Albeni, B.C., Del Bigio, M.R., Martin, M., 2013. Neurofibrillary tangles and plaques are not accompanied by white matter pathology in aged triple transgenic-Alzheimer disease mice. *Magn. Reson. Imaging* 31, 1515–1521. doi:10.1016/j.mri.2013.06.013
- Kiefer, C., Brockhaus, L., Cattapan-Ludewig, K., Ballinari, P., Burren, Y., Schroth, G., Wiest, R., 2009. Multi-parametric classification of Alzheimer's disease and mild cognitive impairment: The impact of quantitative magnetization transfer MR imaging. *Neuroimage* 48, 657–667. doi:10.1016/j.neuroimage.2009.07.005
- Koay, C.G., Chang, L.C., Carew, J.D., Pierpaoli, C., Basser, P.J., 2006. A unifying theoretical and algorithmic framework for least squares methods of estimation in diffusion tensor imaging. *J. Magn. Reson.* 182, 115–125. doi:10.1016/j.jmr.2006.06.020
- Lambert, M.P., Barlow, A.K., Chromy, B.A., Edwards, C., Freed, R., Liosatos, M., Morgan, T.E., Rozovsky, I., Trommer, B., Viola, K.L., Wals, P., Zhang, C., Finch, C.E., Krafft, G.A., Klein, W.L., 1998. Diffusible, nonfibrillar ligands derived from Abeta1-42 are potent central nervous system neurotoxins. *Proc. Natl. Acad. Sci. U. S. A.* 95, 6448–53. doi:10.1073/pnas.95.11.6448

- Lanz, T.A., Carter, D.B., Merchant, K.M., 2003. Dendritic spine loss in the hippocampus of young PDAPP and Tg2576 mice and its prevention by the ApoE2 genotype. *Neurobiol. Dis.* 13, 246–253. doi:10.1016/S0969-9961(03)00079-2
- Lau, J.C., Lerch, J.P., Sled, J.G., Henkelman, R.M., Evans, A.C., Bedell, B.J., 2008. Longitudinal neuroanatomical changes determined by deformation-based morphometry in a mouse model of Alzheimer's disease. *Neuroimage* 42, 19–27. doi:10.1016/j.neuroimage.2008.04.252
- Le Bihan, D., Breton, E., Lallemand, D., Grenier, P., Cabanis, E., Laval-Jeantet, M., 1986. MR imaging of intravoxel incoherent motions: application to diffusion and perfusion in neurologic disorders. *Radiology* 161, 401–407. doi:10.1148/radiology.161.2.3763909
- Leemans, A., Jones, D.K., 2009. The B-matrix must be rotated when correcting for subject motion in DTI data. *Magn. Reson. Med.* 61, 1336–1349. doi:10.1002/mrm.21890
- Marusak, S.B., Thuret, S., 2014. Why looking at the whole hippocampus is not enough - a critical role for anteroposterior axis, subfield and activation analyses to enhance productivity of hippocampal changes for Alzheimer's disease diagnosis. *Front. Cell. Neurosci.* 8, 95. doi: 10.3389/fncel.2014.00095
- Nir, T.M., Jahanshad, N., Villalon-Reina, J.E., Toga, A.W., Jack, C.R., Weiner, M.W., Thompson, P.M., 2013. Effectiveness of regional DTI measures in distinguishing Alzheimer's disease, MCI, and normal aging. *NeuroImage Clin.* 3, 180–195. doi:10.1016/j.nicl.2013.07.006
- Paxinos, G., Franklin, K.B.J., 2001. The mouse brain in stereotaxic coordinates. *Acad. Press* 1–350.
- Pérez-Torres, C.J., Reynolds, J.O., Pautler, R.G., 2014. Use of magnetization transfer contrast MRI to detect early molecular pathology in Alzheimer's disease. *Magn. Reson. Med.* 71, 333–338. doi:10.1002/mrm.24665
- Perona, P., Malik, J., 1990. Scale-space and edge detection using anisotropic diffusion. *IEEE Trans. Pattern Anal. Mach. Intell.* 12. doi:10.1109/34.56205
- Pini, L., Pievani, M., Bocchetta, M., Altomare, D., Bosco, P., Cavedo, E., Galluzzi, S., Marizzoni, M., Frisoni, G.B., 2016. Brain atrophy in Alzheimer's disease and aging. *Ageing Res. Rev.* 30, 24–48. doi:10.1016/j.arr.2016.01.002
- Ramani, A., Dalton, C., Miller, D.H., Tofts, P.S., Barker, G.J., 2002. Precise estimate of fundamental in-vivo MT parameters in human brain in clinically feasible times. *Magn. Reson. Imaging* 20, 721–731. doi:10.1016/S0730-725X(02)00598-2
- Ridha, B.H., Tozer, D.J., Symms, M.R., Stockton, K.C., Lewis, E.B., Siddique, M.M., MacManus, D.G., Rossor, M.N., Fox, N.C., Tofts, P.S., 2007. Quantitative magnetization transfer imaging in Alzheimer disease. *Radiology* 244, 832–837. doi:10.1148/radiol.2443061128
- Ropele, S., Schmidt, R., Enzinger, C., Windisch, M., Martinez, N.P., Fazekas, F., 2012. Longitudinal magnetization transfer imaging in mild to severe Alzheimer disease. *AJNR. Am. J. Neuroradiol.* 33, 570–5. doi:10.3174/ajnr.A2812

- Rössler, M., Zarski, R., Bohl, J., Ohm, T.G., 2002. Stage-dependent and sector-specific neuronal loss in hippocampus during alzheimer's disease. *Acta Neuropathol.* 103, 363–369. doi:10.1007/s00401-001-0475-7
- Scheenstra, A.E., van de Ven, R.C., van der Weerd, L., van den Maagdenberg, A.M., Dijkstra, J., Reiber, J.H., 2009. Automated segmentation of in vivo and ex vivo mouse brain magnetic resonance images. *Mol Imaging* 8, 35–44.
- Schmierer, K., Wheeler-Kingshott, C.A.M., Tozer, D.J., Boulby, P.A., Parkes, H.G., Yousry, T.A., Scaravilli, F., Barker, G.J., Tofts, P.S., Miller, D.H., 2008. Quantitative magnetic resonance of postmortem multiple sclerosis brain before and after fixation. *Magn. Reson. Med.* 59, 268–277. doi:10.1002/mrm.21487
- Shepherd, T.M., Ozarslan, E., King, M.A., Mareci, T.H., Blackband, S.J., 2006. Structural insights from high-resolution diffusion tensor imaging and tractography of the isolated rat hippocampus. *Neuroimage* 32, 1499–1509. doi:10.1016/j.neuroimage.2006.04.210
- Shepherd, T.M., Thelwall, P.E., Stanisz, G.J., Blackband, S.J., 2009. Aldehyde fixative solutions alter the water relaxation and diffusion properties of nervous tissue. *Magn. Reson. Med.* 62, 26–34. doi:10.1002/mrm.21977
- Song, S.-K., Kim, J.H., Lin, S.-J., Brendza, R.P., Holtzman, D.M., 2004. Diffusion tensor imaging detects age-dependent white matter changes in a transgenic mouse model with amyloid deposition. *Neurobiol. Dis.* 15, 640–647. doi:10.1016/j.nbd.2003.12.003
- Song, S.-K., Sun, S.-W., Ramsbottom, M.J., Chang, C., Russell, J., Cross, A.H., 2002. Demyelination revealed through MRI as increased radial (but unchanged axial) diffusion of water. *Neuroimage* 17, 1429–1436. doi:10.1006/nimg.2002.1267
- Song, S.K., Yoshino, J., Le, T.Q., Lin, S.J., Sun, S.W., Cross, A.H., Armstrong, R.C., 2005. Demyelination increases radial diffusivity in corpus callosum of mouse brain. *Neuroimage* 26, 132–140. doi:10.1016/j.neuroimage.2005.01.028
- Spencer, N.G., Bridges, L.R., Elderfield, K., Amir, K., Austen, B., Howe, F.A., 2013. Quantitative evaluation of MRI and histological characteristics of the 5xFAD Alzheimer mouse brain. *Neuroimage* 76, 108–115. doi:10.1016/j.neuroimage.2013.02.071
- Sperling, R.A., Aisen, P.S., Beckett, L.A., Bennett, D., Craft, S., Fagan, A.M., Iwatsubo, T., Jack, C.R., Kaye, J., Montine, T.J., Park, D.C., Reiman, E.M., Rowe, C.C., Siemers, E., Stern, Y., Yaffe, K., Carrillo, M.C., Thies, B., Morrison-Bogorad, M., Wagster, M. V., Phelps, C.H., 2011. Toward defining the preclinical stages of Alzheimer's disease: Recommendations from the National Institute on Aging and the Alzheimer's Association workgroup. *Alzheimer's Dement.* 7, 280–292. doi:10.1016/j.jalz.2011.03.003
- Stoub, T.R., DeToledo-Morrell, L., Dickerson, B.C., 2014. Parahippocampal white matter volume predicts Alzheimer's disease risk in cognitively normal old adults. *Neurobiol. Aging* 35, 1855–1861. doi:10.1016/j.neurobiolaging.2014.01.153
- Sun, S.-W., Liang, H.-F., Mei, J., Xu, D., Shi, W.-X., 2014. In vivo diffusion tensor imaging of amyloid- β -induced white matter damage in mice. *J. Alzheimers. Dis.* 38, 93–101. doi:10.3233/JAD-130236

- Sun, S.W., Liang, H.F., Trinkaus, K., Cross, A.H., Armstrong, R.C., Song, S.K., 2006. Noninvasive detection of cuprizone induced axonal damage and demyelination in the mouse corpus callosum. *Magn. Reson. Med.* 55, 302–308. doi:10.1002/mrm.20774
- Sun, S.W., Liang, H.F., Xie, M., Oyoyo, U., Lee, A., 2009. Fixation, not death, reduces sensitivity of DTI in detecting optic nerve damage. *Neuroimage* 44, 611–619. doi:10.1016/j.neuroimage.2008.10.032
- Sun, S.W., Neil, J.J., Liang, H.F., He, Y.Y., Schmidt, R.E., Hsu, C.Y., Song, S.K., 2005. Formalin fixation alters water diffusion coefficient magnitude but not anisotropy in infarcted brain. *Magn. Reson. Med.* 53, 1447–1451. doi:10.1002/mrm.20488
- Teipel, S.J., Grothe, M., Lista, S., Toschi, N., Garaci, F.G., Hampel, H., 2013. Relevance of magnetic resonance imaging for early detection and diagnosis of Alzheimer disease. *Med. Clin. North Am.* 97, 399–424. doi:10.1016/j.mcna.2012.12.013
- Thiessen, J.D., Zhang, Y., Zhang, H., Wang, L., Buist, R., Del Bigio, M.R., Kong, J., Li, X.M., Martin, M., 2013. Quantitative MRI and ultrastructural examination of the cuprizone mouse model of demyelination. *NMR Biomed.* 26, 1562–1581. doi:10.1002/nbm.2992
- Walsh, D.M., Klyubin, I., Fadeeva, J. V, Cullen, W.K., Anwyl, R., Wolfe, M.S., Rowan, M.J., Selkoe, D.J., 2002. Naturally secreted oligomers of amyloid beta protein potently inhibit hippocampal long-term potentiation in vivo. *Nature* 416, 535–539. doi:10.1038/416535a
- West, M.J., Coleman, P.D., Flood, D.G., Troncoso, J.C., 1994. Differences in the pattern of hippocampal neuronal loss in normal ageing and Alzheimer's disease. *Lancet* 344, 769–772. doi:10.1016/S0140-6736(94)92338-8
- Wolff, S.D., Balaban, R.S., 1989. Magnetization transfer contrast (MTC) and tissue water proton relaxation in vivo. *Magn. Reson. Med.* 10, 135–144. doi:10.1002/mrm.1910100113
- Zhang, J., Jones, M. V., McMahon, M.T., Mori, S., Calabresi, P.A., 2012. In vivo and ex vivo diffusion tensor imaging of cuprizone-induced demyelination in the mouse corpus callosum. *Magn. Reson. Med.* 67, 750–759. doi:10.1002/mrm.23032
- Zhang, J., van Zijl, P.C.M., Mori, S., 2002. Three-dimensional diffusion tensor magnetic resonance microimaging of adult mouse brain and hippocampus. *Neuroimage* 15, 892–901. doi:10.1006/nimg.2001.1012

Figure Titles

Figure 1. Slice geometry of the coronal slices used for all imaging. The three slices of interest are outlined in magenta and labeled as rostral, middle, and caudal. The middle slice was positioned 2.50 mm caudal to the anterior commissure and had a 0.5 mm slice thickness, with 1.0 mm spacing between slices.

Figure 2. Quantitative MRI maps of the middle slice of a representative Tg2576 mouse brain. The scale from black to white is given below each map. Various white matter tracts are visible with varying contrast in all of the different quantitative MRI maps, but cell layers within the gray matter of the hippocampus proper and dentate gyrus are only visible in FA and DEC maps.

Figure 3. DEC maps of a representative Tg2576 mouse brain from each of the three slices. The red, green, and blue colours each represent the x-, y-, and z- directions of water diffusion respectively, and the brightness of the pixels corresponds to anisotropy. The entire hippocampus proper and dentate gyrus are outlined together in white in (A). Hippocampal strata ROIs are outlined in white and indicated by arrows in (B), and white matter ROIs are similarly labelled in (C). Note that all ROIs appear in both left and right hemispheres but are labelled here only on the left. The mean value of all metrics calculated is the spatial average of both the left and right for all ROIs except the corpus callosum, which spans the midline. **ROIs: Hippocampal:** radiatum (H_{rad}) and lacunosum-moleculare (H_{lm}) layers of the hippocampus; top/bottom molecular (DG_{mt}/DG_{mb}) and granular/polymorph (DG_{gp}) layers of the dentate gyrus. **White matter:** cingulum (cg), corpus callosum (cc), fimbria of the hippocampus (fi), external capsule (ec), brachium of the superior colliculus (bsc), and dorsal hippocampal commissure (dhc).

Figure 4. Unsaturated DEC maps of a representative Tg2576 mouse brain with regions of interest coloured-in to indicate statistically significant difference between transgenic and control mice in multiple metrics. Results are presented from the whole hippocampal region (A), each hippocampal cell layer (B), and white matter regions (C). Hippocampal cell layers (B) appear in each of the rostral (leftmost), middle, and caudal (rightmost) slices, whereas the white matter regions (C) appear in only one slice. All regions are outlined in white and are filled in if they contain significant group differences in T_1 and FA (yellow), T_1 and R_A (magenta), or a combination of T_1 , FA and R_A (cyan). ($p < 0.05$ using a one-way ANOVA).

Figure 5. Immunohistochemical staining for $A\beta$ in a representative 7.5-month-old Tg2576 mouse hippocampus, at rostral (A), middle (B), and caudal (C) levels. $A\beta$ deposition (brown) as detected by anti- $A\beta$ antibody 82E1, was evident as extracellular plaques (indicated by arrows) in the hippocampal and dentate gyrus cell layers. Intracellular staining for $A\beta$ was not apparent, and the plaques appeared diffuse upon magnification (D).

Appendix

Table A1. Relaxation, DT, and qMT measurements in rostral, middle, and caudal slices of the hippocampus, in control mice (CON, n=6) and Tg2576 transgenic mice (APP, n=6).

ROI	CON		APP			CON		APP	
	T ₁ (s)		FA			R _A (s ⁻¹)			
Rostral	1.47 ± 0.08	1.38 ± 0.06	0.15 ± 0.02	0.29 ± 0.04	*	0.66 ± 0.04	0.71 ± 0.03		
Middle	1.53 ± 0.07	1.40 ± 0.10	0.16 ± 0.03	0.23 ± 0.03	*	0.64 ± 0.03	0.70 ± 0.06		
Caudal	1.46 ± 0.05	1.40 ± 0.06	0.21 ± 0.03	0.25 ± 0.04	*	0.67 ± 0.02	0.71 ± 0.03		
	MD (μm ² /ms)		λ _{//} (μm ² /ms)			λ _⊥ (μm ² /ms)			
Rostral	0.37 ± 0.05	0.34 ± 0.02	0.43 ± 0.07	0.41 ± 0.02		0.34 ± 0.05	0.31 ± 0.02		
Middle	0.36 ± 0.05	0.33 ± 0.02	0.42 ± 0.06	0.41 ± 0.02		0.33 ± 0.04	0.29 ± 0.02		
Caudal	0.30 ± 0.06	0.29 ± 0.03	0.36 ± 0.06	0.36 ± 0.03		0.27 ± 0.05	0.25 ± 0.03		
	RM ⁰ _A (s ⁻¹)		T ₂ ^A (ms)			T ₂ ^B (μs)			
Rostral	34 ± 5	30 ± 4	72 ± 9	83 ± 20		7.2 ± 0.4	7.5 ± 0.4		
Middle	33 ± 5	30 ± 5	72 ± 8	80 ± 20		7.3 ± 0.5	7.6 ± 0.3		
Caudal	31 ± 7	30 ± 5	70 ± 10	86 ± 10	*	7.1 ± 0.7	7.6 ± 0.4		
	f (x10 ⁻¹)								
Rostral	0.56 ± 0.03	0.55 ± 0.05							
Middle	0.56 ± 0.02	0.55 ± 0.03							
Caudal	0.63 ± 0.06	0.55 ± 0.03			*				

*difference between control and transgenic mice is statistically significant (p<0.05) in ANOVA.

Table A2. Relaxation, DT, and qMT measurements in rostral (R), middle (M), and caudal (C) slices of five hippocampal cell layers, in control mice (CON, n=6) and Tg2576 transgenic mice (APP, n=6). Cell layers include the stratum radiatum of the hippocampus (H_{rad}), stratum lacunosum moleculare of the hippocampus (H_{lm}), top molecular layer of the dentate gyrus (DG_{mt}), bottom molecular layer of the dentate gyrus (DG_{mb}), and granule and polymorph layers of the dentate gyrus (DG_{gp}).

ROI	CON		APP			CON		APP			CON		APP		
	T_1 (s)		FA			R_A (s^{-1})									
H_{rad}	R	1.45 ± 0.08	1.36 ± 0.06	*		0.14 ± 0.02	0.16 ± 0.03		0.67 ± 0.04	0.72 ± 0.03	*		0.65 ± 0.03	0.72 ± 0.05	*
	M	1.49 ± 0.07	1.37 ± 0.09	*		0.16 ± 0.04	0.18 ± 0.03		0.67 ± 0.03	0.71 ± 0.03	*		0.67 ± 0.03	0.71 ± 0.03	*
	C	1.44 ± 0.05	1.38 ± 0.05			0.18 ± 0.05	0.20 ± 0.04		0.67 ± 0.03	0.71 ± 0.03	*		0.67 ± 0.03	0.71 ± 0.03	*
H_{lm}	R	1.47 ± 0.07	1.39 ± 0.07			0.15 ± 0.04	0.20 ± 0.05		0.67 ± 0.04	0.71 ± 0.04			0.67 ± 0.04	0.71 ± 0.04	
	M	1.56 ± 0.05	1.40 ± 0.10	*		0.15 ± 0.03	0.21 ± 0.04	*	0.62 ± 0.02	0.69 ± 0.06	*		0.62 ± 0.02	0.69 ± 0.06	*
	C	1.47 ± 0.05	1.41 ± 0.06			0.20 ± 0.03	0.24 ± 0.02	*	0.66 ± 0.03	0.70 ± 0.03	*		0.66 ± 0.03	0.70 ± 0.03	*
DG_{mt}	R	1.47 ± 0.07	1.38 ± 0.05	*		0.13 ± 0.03	0.18 ± 0.05	*	0.66 ± 0.04	0.71 ± 0.03	*		0.66 ± 0.04	0.71 ± 0.03	*
	M	1.51 ± 0.06	1.40 ± 0.10	*		0.15 ± 0.04	0.22 ± 0.04	*	0.64 ± 0.03	0.70 ± 0.06	*		0.64 ± 0.03	0.70 ± 0.06	*
	C	1.47 ± 0.06	1.40 ± 0.06	*		0.16 ± 0.02	0.22 ± 0.04	*	0.65 ± 0.03	0.70 ± 0.03	*		0.65 ± 0.03	0.70 ± 0.03	*
DG_{mb}	R	1.49 ± 0.07	1.40 ± 0.06	*		0.14 ± 0.02	0.18 ± 0.04		0.65 ± 0.03	0.68 ± 0.03	*		0.65 ± 0.03	0.68 ± 0.03	*
	M	1.55 ± 0.06	1.40 ± 0.10			0.15 ± 0.02	0.21 ± 0.03	*	0.62 ± 0.03	0.68 ± 0.06	*		0.62 ± 0.03	0.68 ± 0.06	*
	C	1.49 ± 0.05	1.43 ± 0.06			0.21 ± 0.04	0.23 ± 0.05		0.65 ± 0.02	0.70 ± 0.03			0.65 ± 0.02	0.70 ± 0.03	
DG_{gp}	R	1.46 ± 0.07	1.39 ± 0.06			0.15 ± 0.04	0.22 ± 0.05	*	0.67 ± 0.04	0.71 ± 0.03			0.67 ± 0.04	0.71 ± 0.03	
	M	1.51 ± 0.07	1.40 ± 0.10			0.17 ± 0.04	0.26 ± 0.03	*	0.64 ± 0.03	0.70 ± 0.06	*		0.64 ± 0.03	0.70 ± 0.06	*
	C	1.43 ± 0.04	1.38 ± 0.06			0.27 ± 0.07	0.36 ± 0.06	*	0.68 ± 0.02	0.71 ± 0.03	*		0.68 ± 0.02	0.71 ± 0.03	*
	MD ($\mu\text{m}^2/\text{ms}$)					λ_{\parallel} ($\mu\text{m}^2/\text{ms}$)					λ_{\perp} ($\mu\text{m}^2/\text{ms}$)				
H_{rad}	R	0.37 ± 0.06	0.35 ± 0.01			0.42 ± 0.07	0.40 ± 0.01		0.34 ± 0.05	0.32 ± 0.01			0.33 ± 0.05	0.31 ± 0.02	
	M	0.36 ± 0.05	0.34 ± 0.02			0.42 ± 0.06	0.41 ± 0.02		0.33 ± 0.05	0.31 ± 0.02			0.33 ± 0.05	0.31 ± 0.02	
	C	0.30 ± 0.05	0.29 ± 0.03			0.36 ± 0.06	0.34 ± 0.03		0.28 ± 0.05	0.26 ± 0.03			0.28 ± 0.05	0.26 ± 0.03	
H_{lm}	R	0.38 ± 0.06	0.34 ± 0.03			0.44 ± 0.08	0.41 ± 0.02		0.35 ± 0.06	0.31 ± 0.03			0.35 ± 0.06	0.31 ± 0.03	
	M	0.35 ± 0.07	0.33 ± 0.02			0.40 ± 0.08	0.40 ± 0.03		0.32 ± 0.06	0.30 ± 0.02			0.32 ± 0.06	0.30 ± 0.02	
	C	0.29 ± 0.05	0.27 ± 0.03			0.34 ± 0.06	0.33 ± 0.05		0.26 ± 0.05	0.24 ± 0.03			0.26 ± 0.05	0.24 ± 0.03	
DG_{mt}	R	0.37 ± 0.05	0.34 ± 0.02			0.42 ± 0.07	0.40 ± 0.03		0.35 ± 0.05	0.30 ± 0.02			0.35 ± 0.05	0.30 ± 0.02	
	M	0.36 ± 0.05	0.34 ± 0.03			0.42 ± 0.06	0.41 ± 0.03		0.34 ± 0.04	0.30 ± 0.03			0.34 ± 0.04	0.30 ± 0.03	
	C	0.29 ± 0.06	0.28 ± 0.03			0.34 ± 0.06	0.35 ± 0.03		0.27 ± 0.05	0.25 ± 0.02			0.27 ± 0.05	0.25 ± 0.02	
DG_{mb}	R	0.36 ± 0.05	0.33 ± 0.02			0.41 ± 0.07	0.39 ± 0.02		0.33 ± 0.04	0.30 ± 0.02			0.33 ± 0.04	0.30 ± 0.02	
	M	0.34 ± 0.05	0.31 ± 0.03			0.39 ± 0.05	0.37 ± 0.04		0.32 ± 0.04	0.27 ± 0.03			0.32 ± 0.04	0.27 ± 0.03	
	C	0.29 ± 0.06	0.28 ± 0.03			0.35 ± 0.06	0.34 ± 0.04		0.26 ± 0.06	0.24 ± 0.03			0.26 ± 0.06	0.24 ± 0.03	
DG_{gp}	R	0.37 ± 0.05	0.35 ± 0.01			0.43 ± 0.08	0.43 ± 0.02		0.34 ± 0.04	0.31 ± 0.02			0.34 ± 0.04	0.31 ± 0.02	
	M	0.36 ± 0.05	0.33 ± 0.02			0.42 ± 0.07	0.42 ± 0.02		0.32 ± 0.04	0.29 ± 0.02			0.32 ± 0.04	0.29 ± 0.02	
	C	0.32 ± 0.06	0.31 ± 0.03			0.41 ± 0.09	0.44 ± 0.04		0.27 ± 0.06	0.25 ± 0.03			0.27 ± 0.06	0.25 ± 0.03	

(continued on next page)

Table A2 continued.

ROI	CON		APP			CON		APP	
	RM ⁰ _A (s ⁻¹)		T ₂ ^A (ms)			T ₂ ^B (μs)			
H _{rad}	R	33 ± 5	30 ± 4	80 ± 10	90 ± 20	7.1 ± 0.4	7.4 ± 0.3		
	M	34 ± 5	32 ± 6	74 ± 8	90 ± 20	7.2 ± 0.3	7.5 ± 0.3		
	C	31 ± 8	30 ± 5	70 ± 1	90 ± 20	6.9 ± 0.9	7.5 ± 0.4	*	
H _{lm}	R	33 ± 5	28 ± 4	80 ± 10	90 ± 20	7.1 ± 0.4	7.4 ± 0.3		
	M	33 ± 3	33 ± 7	70 ± 10	90 ± 20	7.4 ± 0.4	7.7 ± 0.4		
	C	30 ± 8	30 ± 5	70 ± 10	90 ± 20	6.9 ± 0.9	7.7 ± 0.3	*	
DG _{mt}	R	33 ± 5	31 ± 4	73 ± 8	90 ± 30	7.2 ± 0.4	7.4 ± 0.4		
	M	32 ± 5	30 ± 5	76 ± 7	80 ± 20	7.3 ± 0.5	7.5 ± 0.3		
	C	31 ± 7	30 ± 5	69 ± 9	90 ± 10	7.1 ± 0.6	7.6 ± 0.3	*	
DG _{mb}	R	34 ± 6	30 ± 4	70 ± 10	80 ± 20	7.2 ± 0.5	7.6 ± 0.3		
	M	31 ± 4	29 ± 5	73 ± 8	80 ± 20	7.5 ± 0.4	7.6 ± 0.4		
	C	30 ± 6	30 ± 5	69 ± 9	80 ± 10	7.2 ± 0.5	7.7 ± 0.4	*	
DG _{gp}	R	34 ± 5	31 ± 4	70 ± 10	78 ± 20	7.2 ± 0.5	7.6 ± 0.4		
	M	33 ± 6	30 ± 5	70 ± 10	80 ± 20	7.3 ± 0.5	7.6 ± 0.3		
	C	31 ± 7	31 ± 5	68 ± 9	80 ± 10	7.1 ± 0.5	7.6 ± 0.4	*	
$f(x10^{-1})$									
H _{rad}	R	0.54 ± 0.02	0.53 ± 0.07						
	M	0.53 ± 0.04	0.50 ± 0.05						
	C	0.63 ± 0.07	0.53 ± 0.04	*					
H _{lm}	R	0.53 ± 0.02	0.53 ± 0.03						
	M	0.53 ± 0.05	0.50 ± 0.05						
	C	0.62 ± 0.09	0.54 ± 0.06						
DG _{mt}	R	0.56 ± 0.04	0.54 ± 0.05						
	M	0.54 ± 0.02	0.53 ± 0.03						
	C	0.62 ± 0.05	0.55 ± 0.03	*					
DG _{mb}	R	0.56 ± 0.06	0.56 ± 0.05						
	M	0.57 ± 0.02	0.56 ± 0.03						
	C	0.62 ± 0.04	0.56 ± 0.03	*					
DG _{gp}	R	0.58 ± 0.06	0.57 ± 0.05						
	M	0.57 ± 0.04	0.57 ± 0.03						
	C	0.64 ± 0.05	0.57 ± 0.02	*					

*difference between control and transgenic mice is statistically significant (p<0.05) in ANOVA.

Table A3. Relaxation, DT, and qMT measurements in six white matter tracts, in control mice (CON, n=6) and Tg2576 transgenic mice (APP, n=6). ROIs include the cingulum (cg), corpus callosum (cc), fimbria of the hippocampus (fi), external capsule (ec), brachium of the superior colliculus (bsc), and dorsal hippocampal commissure (dhc).

ROI	CON		APP			CON		APP		
	T_1 (s)		FA			R_A (s ⁻¹)				
cg	1.41 ± 0.05	1.34 ± 0.05	*	0.48 ± 0.06	0.59 ± 0.05	*	26.7 ± 4.8	23.3 ± 5.0	*	
cc	1.50 ± 0.06	1.43 ± 0.02	*	0.49 ± 0.05	0.6 ± 0.1		24.6 ± 3.9	23.6 ± 3.9	*	
fi	1.53 ± 0.05	1.50 ± 0.06	*	0.45 ± 0.07	0.52 ± 0.08		28.7 ± 4.3	25.2 ± 4.1		
ec	1.52 ± 0.05	1.40 ± 0.10	*	0.53 ± 0.07	0.61 ± 0.08		24.3 ± 4.6	22.9 ± 4.5	*	
bsc	1.54 ± 0.06	1.40 ± 0.10	*	0.38 ± 0.08	0.47 ± 0.09		26.7 ± 5.3	25.5 ± 4.8		
dhc	1.48 ± 0.05	1.38 ± 0.05	*	0.59 ± 0.07	0.69 ± 0.05	*	25.6 ± 4.9	26.5 ± 5.5	*	
	MD (μm ² /ms)			$\lambda_{//}$ (μm ² /ms)			λ_{\perp} (μm ² /ms)			
cg	0.26 ± 0.06	0.26 ± 0.02		0.41 ± 0.08	0.44 ± 0.03		0.19 ± 0.05	0.16 ± 0.02		
cc	0.23 ± 0.06	0.21 ± 0.02		0.36 ± 0.09	0.36 ± 0.05		0.16 ± 0.04	0.13 ± 0.03		
fi	0.29 ± 0.05	0.28 ± 0.02		0.44 ± 0.06	0.45 ± 0.05		0.22 ± 0.05	0.20 ± 0.03		
ec	0.26 ± 0.06	0.25 ± 0.03		0.41 ± 0.09	0.43 ± 0.06		0.18 ± 0.05	0.16 ± 0.03		
bsc	0.29 ± 0.04	0.26 ± 0.03		0.41 ± 0.07	0.39 ± 0.04		0.23 ± 0.04	0.19 ± 0.04		
dhc	0.26 ± 0.05	0.25 ± 0.03		0.46 ± 0.08	0.49 ± 0.05		0.16 ± 0.04	0.13 ± 0.02		
	RM^0_A (s ⁻¹)			T_2^A (ms)			T_2^B (μs)			
cg	8.1 ± 0.3	8.6 ± 0.5		52 ± 5	70 ± 20		8.1 ± 0.3	8.6 ± 0.5	*	
cc	8.3 ± 0.4	8.6 ± 0.4		57 ± 4	70 ± 20		8.3 ± 0.4	8.6 ± 0.4		
fi	8.0 ± 0.5	8.3 ± 0.4		67 ± 7	80 ± 20		8.0 ± 0.5	8.3 ± 0.4		
ec	8.4 ± 0.5	8.7 ± 0.5		65 ± 7	80 ± 10		8.4 ± 0.5	8.7 ± 0.5		
bsc	7.9 ± 0.5	8.3 ± 0.3		70 ± 10	80 ± 10		7.9 ± 0.5	8.0 ± 0.3		
dhc	8.2 ± 0.4	8.4 ± 0.4		58 ± 9	70 ± 10		8.2 ± 0.4	8.4 ± 0.4		
	f (x10 ⁻¹)									
cg	0.85 ± 0.07	0.87 ± 0.09								
cc	0.84 ± 0.07	0.84 ± 0.07								
fi	0.69 ± 0.04	0.67 ± 0.05								
ec	0.81 ± 0.05	0.84 ± 0.02								
bsc	0.68 ± 0.06	0.69 ± 0.03								
dhc	0.80 ± 0.06	0.76 ± 0.07								

*difference between control and transgenic mice is statistically significant (p<0.05) in ANOVA.